Monthly Notices
of the
ROYAL ASTRONOMICAL SOCIETY

MNRAS **439,** 416–431 (2014)
Advance Access publication 2014 February 6

doi:10.1093/mnras/stu020

Stellar populations in central cluster galaxies: the influence of cooling flows⋆

S. I. Loubser†

Centre for Space Research, North-West University, Potchefstroom 2520, South Africa

Accepted 2013 December 19. Received 2013 December 19; in original form 2013 September 12

ABSTRACT

We present detailed, high spatial and spectral resolution, long-slit observations of four central cluster galaxies (CCGs; Abell 0085, 0133, 0644 and Ophiuchus) recently obtained on the Southern African Large Telescope. Our sample consists of CCGs with previously observed Hα filaments, and have existing data from the X-ray to radio wavelength regimes available. Here, we present the detailed optical data over a broad wavelength range to probe the spatially resolved kinematics and stellar populations of the stars. We use the PEGASE.HR model with the ELODIE v3.1 stellar library to determine the star formation histories of the galaxies using full spectrum fitting. We perform single stellar population as well as composite stellar population fits to account for more complex star formation histories. Monte Carlo simulations and χ^2 maps are used to check the reliability of the solutions. This, combined with the other multiwavelength data, will form a complete view of the different phases (hot and cold gas and stars) and how they interact in the processes of star formation and feedback detected in central galaxies in cooling flow clusters, as well as the influence of the host cluster. We find small, young stellar components in at least three of the four galaxies, even though two of the three host clusters have zero spectrally derived mass deposition rates from X-ray observations.

Key words: galaxies: clusters: individual: Abell 0085 – galaxies: clusters: individual: Abell 0133 – galaxies: clusters: individual: Abell 0644 – galaxies: clusters: individual: Ophiuchus – galaxies: elliptical and lenticular, cD – galaxies: formation.

1 INTRODUCTION

Cooling flows in galaxy clusters, once thought to be on the order of 100–1000 $M_\odot$ yr^{-1}, are now understood to be depositing cool gas on the order of 1–10 $M_\odot$ yr^{-1} on to the central cluster galaxy (CCG; Voigt & Fabian 2004). It is now generally accepted that some form of feedback [active galactic nuclei (AGN), conduction, etc.] prevents the intracluster medium from cooling, allowing only small amounts of cool gas to accrete on to the CCG. Thus, CCGs lie at the interface where it is crucial to understand the role of feedback and accretion in star formation. Within these cooling-flow CCGs, cool molecular clouds, warm ionized hydrogen and the cooling intracluster medium are related. A complete view of the star formation process incorporates the stars with the gas and an understanding of the processes by which these phases interact, and therefore requires information from several wavelength regimes.

Various previous studies have reported several examples of ongoing star formation in CCGs, in particular those hosted by cooling-flow clusters (Cardiel, Gorgas & Aragón-Salamanca 1998; Crawford et al. 1999; McNamara et al. 2006; Edwards et al. 2007; Bildfell et al. 2008; O'Dea et al. 2008, 2010; Loubser et al. 2009; Pipino et al. 2009; Liu, Mao & Meng 2012). Although active star formation in these central galaxies is compelling, the young populations only contribute a very small mass fraction (Pipino et al. 2009), and it has been shown that star formation in these CCGs is correlated with the cooling time of the gas (Rafferty, McNamara & Nulsen 2008; Liu et al. 2012). Recent studies have even claimed that star-forming central galaxies are exclusively hosted by cooling-flow clusters (Hoffer et al. 2012, and references therein), although not all cooling-flow clusters contain star-forming galaxies. The empirical boundary between clusters that host active central galaxies and clusters that never host them is $K_0 = 30$ keV cm^2, an entropy corresponding to an intracluster medium cooling time of ∼1 Gyr (Voit et al. 2008). The origin of the gas fuelling this star formation is not yet fully understood. Probable explanations include processes involving the cooling flows, but cold gas deposited during a merging event cannot be conclusively eliminated (Bildfell et al. 2008).

With the advent of more accurate methods to fit complex star formation histories (SFHs) from high-quality optical spectroscopy, we are now in a position to directly compare the light/mass fraction of any possible present young stellar population component to the cooling rate of the host cluster.

⋆ Based on observations made with the Southern African Large Telescope (SALT).

† E-mail: ilani.loubser@nwu.ac.za

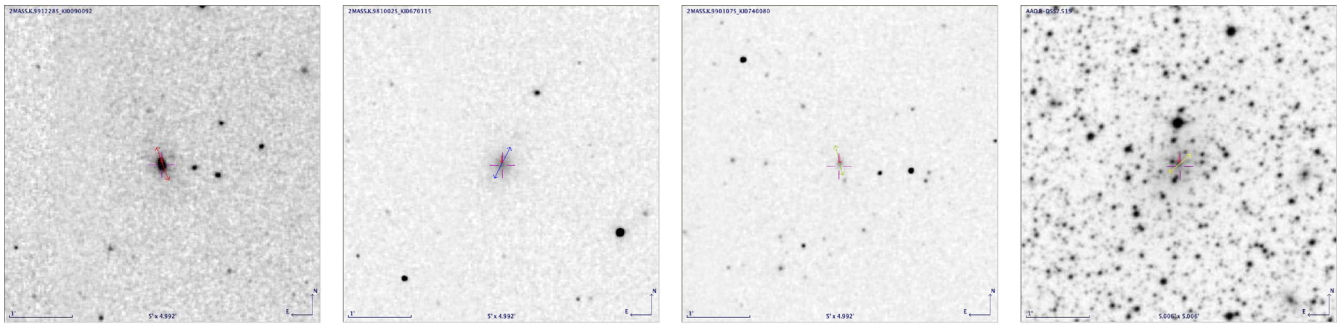

(a) ESO541-013 (b) MCG02-02-086 (c) PGC023233 (d) 2MASXJ17122774-2322108

Figure 1. Slit placements overlaid on DSS images of the four targets (E to the left). The plots show 5 × 5 arcmin^2 field of views.

Table 1. Galaxies observed with the SALT telescope. All four galaxies show extended Hα emission (McDonald et al. 2010). The cluster X-ray temperature (T_X) and classical cooling rates ($\dot{M}$) are from White et al. (1997). The spectrally determined cooling rates are from McDonald et al. (2010). The values for R_{off} are from Edwards et al. (2007) for ESO 541−013 and MCG 02-02-086, and for 2MASX J17122774−2322108 was calculated from information in NED (http://nedwww.ipac.caltech.edu/). This was not possible for Abell 0644, where the CCG is not in the centre of the main cluster and where the coordinates of a corresponding local X-ray maximum were not available.

Object	Cluster	Redshift z	R_{off} (Mpc)	T_X (keV)	Classical cooling rates ($M_\odot$ yr^{-2})	Spectrally determined ($M_\odot$ yr^{-2})	Exposure time (s)
ESO 541−013	Abell 0133	0.057	0.017	3.5	110	0.0	9704
MCG-02-02-086	Abell 0085	0.056	0.046	6.5	108	2.2	6353
PGC 023233	Abell 0644	0.071	–	6.5	136	1.5	6800
2MASX J17122774−2322108	Ophiuchus	0.028	0.019	8.6	41	0.0	14 030

We proposed and obtained long-slit observations of CCGs with confirmed Hα filaments. We selected galaxies with near-infrared [IR; Two Micron All Sky Survey (2MASS)], ultraviolet [UV; *Galaxy Evolution Explorer* (*GALEX*)], X-ray data (*Chandra*) and Very Large Array (VLA) 1.4 GHz fluxes, already available (McDonald et al. 2010). Detailed properties of the host clusters, which are reported to influence the activity in the central galaxy (as described above), such as central cooling times and the offset between the cluster X-ray peak and the central galaxy, have been derived in previous studies and are available in the literature.

These data are complimentary to the emission-line, long-slit spectroscopy (on Keck and Magellan) along the Hα filaments of nine CCGs (not including the four studied here) by McDonald, Veilleux & Rupke (2012). To get maximum possible information, we observed line ratios over a very long wavelength range (around Hα and Hβ) with the slit aligned on, or as close as possible, to the major axis of the galaxy. We can now place the derived information from the stellar population analysis of the optical spectra in context with multiwavelength data over the full spectrum to explain the diverse nature of these galaxies.

We introduce the sample and detail of the data reductions in Sections 2 and 3. We then derive the kinematics as well as the stellar populations in Section 4. We proceed to discuss the four individual cases in Section 5. We summarize the findings of this paper in Section 6. We have used the following set of cosmological parameters: $\Omega_m = 0.3$, $\Omega_\Lambda = 0.7$, $H_0 = 70$ km s^{-1} Mpc^{-1}.

2 SAMPLE

We have chosen our sample of CCGs from the Hα imaging presented in McDonald et al. (2010), who in turn, selected their sample from White, Jones & Forman (1997). McDonald et al. (2010) enforced the cuts: $\delta < +35^\circ$ and $0.025 < z < 0.092$, after which they selected 23 clusters to cover the full range of properties, from very rich clusters with high cooling rates to low-density clusters with very small cooling flows. From their 23 clusters, we selected all the clusters with clearly detected Hα in their centres (albeit filamentary, extended or nuclear emission). In addition, all of these central galaxies have optical imaging, near-IR (2MASS) and UV (*GALEX* data) available. Thereafter, we selected all the central galaxies with detailed X-ray (*Chandra*) data, as well as VLA 1.4 GHz fluxes, available. This resulted in a subsample of 10 galaxies. We observed four of these galaxies with the Gemini Multiobject Spectrograph (GMOS) Integral Field Unit (IFU; as presented in Loubser & Soechting 2013), and four with the Southern African Large Telescope (SALT) Robert Stobie Spectrograph (RSS; as shown in Fig. 1). This does not constitute a complete sample as we merely chose the objects with the most auxiliary information available.

3 OBSERVATIONS AND DATA REDUCTION

The data were obtained with the Robert Stobie Spectrograph (RSS; see Burgh et al. 2003; Kobulnicky et al. 2003) on the SALT telescope between 2011 October and 2012 October (during two

Table 2. Further properties of the CCGs observed on SALT. Radio fluxes are from the NVSS (Condon et al. 1998). The NVSS images are shown in Figs A1–A4.

Object	Extinction (mag) $E(B-V)_{galactic}$	Radio flux (mJy)
ESO 541−013	0.020	167
MCG-02-02-086	0.034	57
PGC 023233	0.109	0
2MASX J17122774−2322108	0.521	29

Table 3. Properties of the CCGs. The PA is given as deg E of N. The slit was placed on, or nearby, the major axis of the galaxies. The half-light radii (r_e) were calculated from the 2MASS catalogue. The last column lists the fraction of the effective half-light radii spanned by the radial profiles measured in this work.

Object	Slit PA (°)	Major axis MA (°)	r_e (arcsec)	ϵ	a_e (arcsec)	Fraction times a_e
ESO 541−013	197	17	10.63	0.40	10.63	0.87
MCG-02-02-086	149	149	12.10	0.22	12.10	0.71
PGC 023233	193	35	6.45	0.14	6.37	0.92
2MASX J17122774−2322108	135	145	20.06	0.28	19.94	0.16

observing semesters and on 24 different nights during dark time under program 2011-2-RSA_OTH-003 and 2012-1-RSA_OTH-003; PI: Ilani Loubser). The rest wavelength of interest is 4860–6731 Å (redshifted to 5000–7300 Å). To achieve this, and to avoid losing essential lines in the CCD gaps, the pg0900 grating was used with 1.2 arcsec slit at a carefully selected central wavelength setting. The targets and exposure times are shown in Table 1 and 2. In addition to the targets, the necessary flat-field and arcs frames were also observed at regular intervals, as well as spectrophotometric standard stars for flux calibration.

The basic reductions were performed with the PYSALT: SALT science pipeline[1] (Crawford et al. 2010), whilst further reductions were done in IRAF.[2] Frames were mosaicked, and the overscan regions were trimmed. Flat-field frames were used to correct for differences in sensitivity both between detector pixels and across the field. The majority of the cosmic rays were rejected in the individual frames before sky subtraction using a cosmic ray rejection routine. The remainder of the cosmic rays were eliminated using the LACOSMIC routine (van Dokkum 2001). The sets of 2D spectra were calibrated in wavelength using the arc lamp spectra. Sky emission lines and continuum were removed by averaging the sky spectrum over a number of spatial pixels to reduce the noise level, before subtracting it from all the spatial pixels. Thus the process adds little extra noise to the result. A spectrophotometric standard star (EG 21) was used to correct the measured counts for the combined transmission of the instrument, telescope and atmosphere as a function of wavelength. We reduced the standard star observation with the same instrument configuration as the corresponding scientific data. A 1D spectrum was extracted by adding the central spatial pixels from the standard star observation, and it was used to convert the measured counts from the galaxy spectra into fluxes with erg cm^{-2} s^{-1} Å^{-1} units. The individual science frames were then combined to produce a one final 2D image per galaxy.

The galaxy and associated error spectra were binned in the spatial direction to ensure a minimum signal-to-noise ratio (S/N) of 30 Å^{-1} in the Hβ region of the spectrum for measurements as a function of radius. An S/N ratio of 30 per bin was chosen to resolve the optimal number of possible points, whilst still having acceptable errors on the measurements. Thus, the spatial cross-sections are broader with increasing radius from the centre of the galaxy up to a maximum of 30 rows. In all the profiles plotted here, the values of the measurements are plotted at the luminosity-weighted centres of the spatial bins used to derive the parameters. A fifth galaxy (PGC 014685) was also observed but with a total exposure time of only 2200 s, and more than 30 rows needed to be added to achieve a S/N of 30 Å^{-1} at Hβ in the centre of the galaxy. Therefore, this galaxy was eliminated from further analysis. All four other galaxies (and their error spectra) consisted of eight or more bins, and reach from $\sim$0.2a_e (2MASX J17122774−2322108) to $\sim$0.9a_e (PGC 023233).

The effective half-light radius was calculated as $a_e = \frac{r_e(1-\epsilon)}{1-\epsilon\ |\cos(|\mathrm{PA}-\mathrm{MA}|)|}$, with ϵ the ellipticity (data from NED), r_e the radius containing half the light of the galaxy (computed from the 2MASS K-band 20th mag arcsec^{-2} isophotal radius as described in Loubser et al. 2008), PA the slit position axis and MA the major axis. These properties are shown in Table 3. For old stellar populations, these half-light radii do not differ much from those derived using the optical bands (Jarrett et al. 2003).

4 KINEMATIC MEASUREMENTS

To detect any possible emission line contamination in the CCG absorption line spectra, we use a combination of the PPXF (Cappellari & Emsellem 2004) and GANDALF (Sarzi et al. 2006) routines as shown in Fig. 2.[3] GANDALF version 1.5 enables a reddening correction to be performed, and incorporates errors. All 985 stars of the MILES stellar library (Sánchez-Blázquez et al. 2006) were used as stellar templates to automatically include α enhancement in the derived optimal template. We followed the procedure described in Sarzi et al. (2006), as well as in Loubser & Soechting (2013). After the kinematics are fixed, a Gaussian template is constructed for each emission line at each iteration, and the best linear combination of both stellar and emission-line templates (with positive weights) is determined.

None of the four CCGs contained measurable emission lines. We only consider the emission-free absorption line spectra for further analysis.

Université de Lyon Spectroscopic analysis Software (ULYSS)[4] is a full spectrum fitting stellar population synthesis code which can be used to determine the stellar atmospheric parameters, star formation and metal enrichment histories of galaxies (Koleva et al. 2009). The entire observed spectrum of an object is fitted against a model which is expressed in the form of a linear combination of non-linear components. These components are given in the form of non-linear functions of ages, metallicities ([Fe/H]), wavelengths and

[1] http://pysalt.salt.ac.za/

[2] IRAF is distributed by the National Optical Astronomy Observatories, which are operated by the Association of Universities for Research in Astronomy, Inc., under cooperative agreement with the National Science Foundation.

[3] We make use of the corresponding PPXF and GANDALF IDL (Interactive Data Language) codes which can be retrieved at http:/www.leidenuniv.nl/sauron/.

[4] Available at http://ulyss.univ-lyon1.fr/.

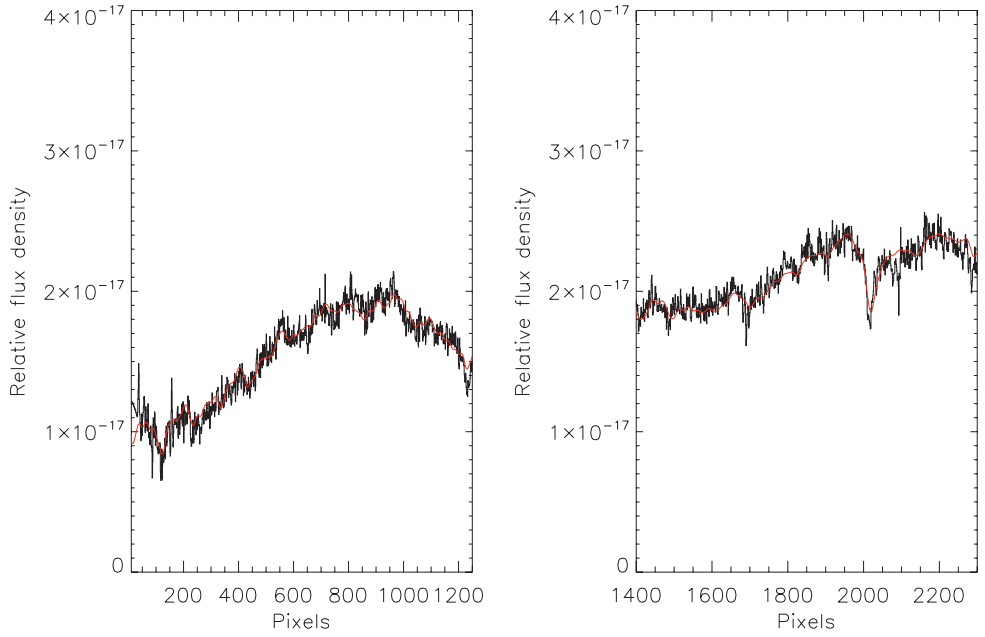

Figure 2. GANDALF fits to the central spectra of MCG-02-02-086 to look for possible weak emission. The red line indicates the combination of stellar spectra from the MILES library that delivered best fit. The panels represent the CCDs.

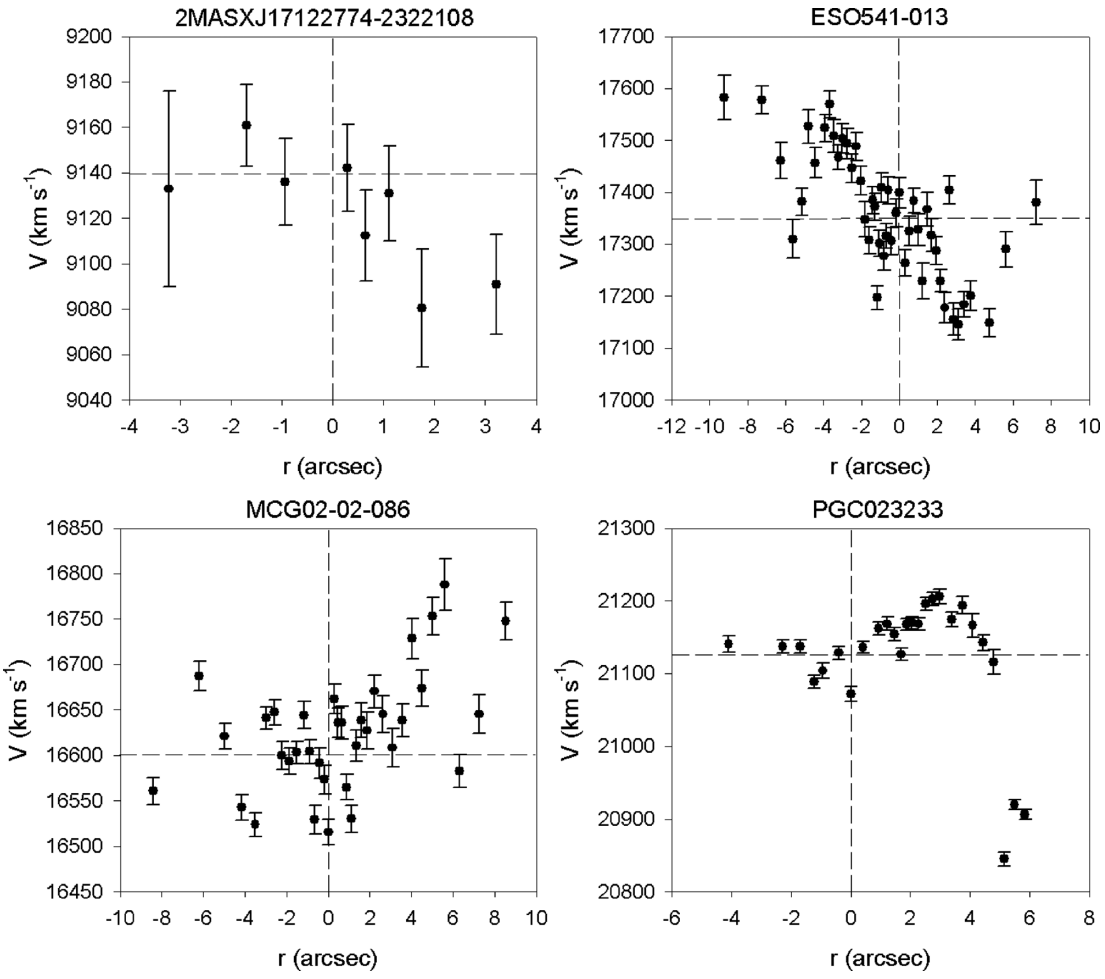

Figure 3. Spatially resolved radial velocities of the four CCGs.

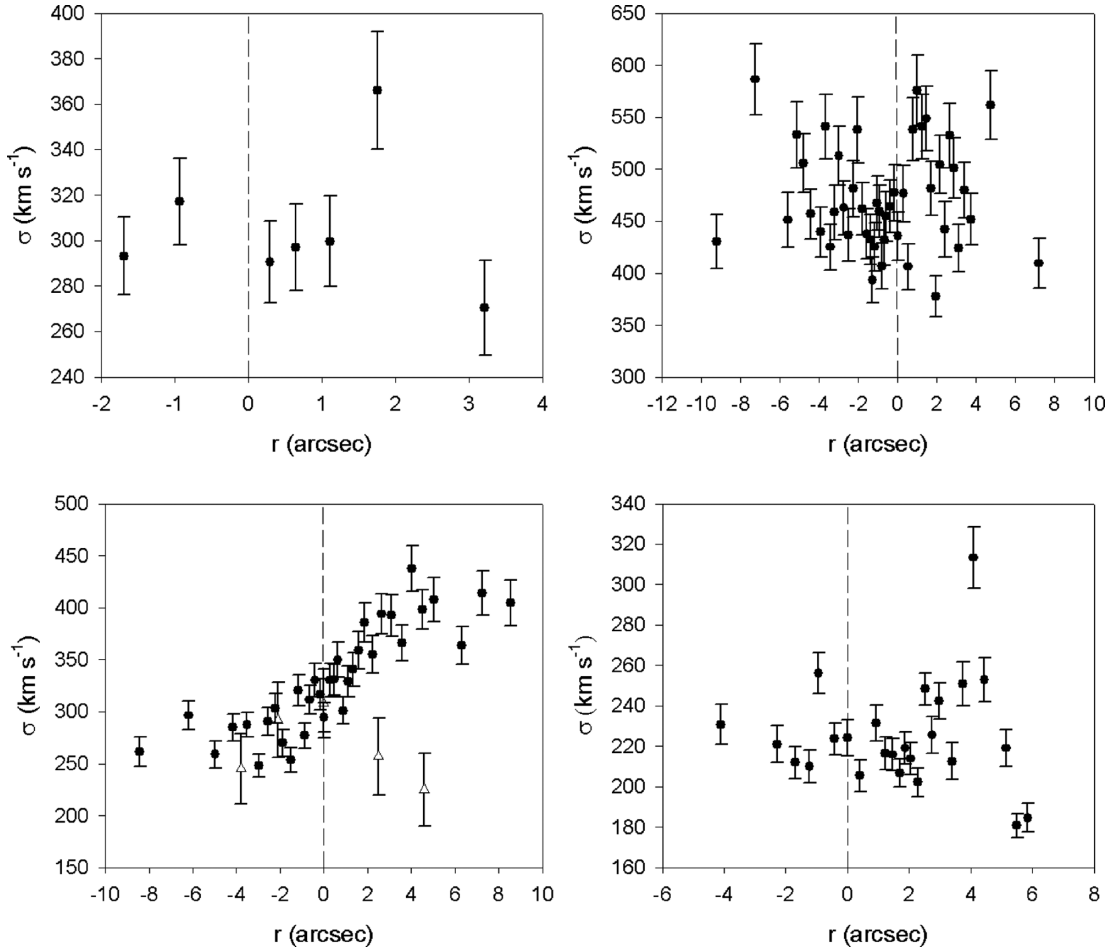

Figure 4. Spatially resolved velocity dispersion measurements of the four CCGs. From left to right, top to bottom: 2MASX J17122774−2322108, ESO 541−013, MCG02-02-086, PGC 023233. The empty triangles in MCG02-02-086 are data from Fisher et al. (1995) also taken along the major axis.

other parameters. Following Bouchard et al. (2010), the models are combined with a line-of-sight velocity distribution (LOSVD) and multiplied with a polynomial to absorb the effects of flux calibration errors and the Galactic extinction which may influence the shape of the spectra (see Viljoen & Loubser 2013 for a detailed demonstration of this method). The ULYSS software package was chosen to analyse the SFHs of the CCGs because this software has features that enable the user to better understand the structure of the parameter space by constructing χ^2 maps which determines the degeneracies and the errors on the parameters (see Koleva et al. 2008).

The PEGASE.HR model with the ELODIE v3.1 stellar library was used (Prugniel et al. 2007). This library covers a wavelength range of 3892–6800 Å and allows the components of the models to be expanded by defining the type of initial mass function (IMF), evolutionary track and star formation rate. The evolutionary tracks of the isochrones are then computed using Padova 1994 (Bertelli et al. 1994). Du et al. (2010) defined these isochrones as being solar scaled at various values of the total metallicity, Z. This version of the stellar library computes the single stellar population (SSPs) with the Salpeter IMF (Salpeter 1955) with a mass of $0.1 \leq M_{\odot} \geq 120$ and a slope of 1.35. This model covers an age range of 0.01; 20.00 Gyr and a [Fe/H] range of −2.30; 0.69 dex. We used a new calibration of this model which includes [Mg/Fe] = 0. Variable α enhancements models are still to be incorporated into the ULYSS software.

The spatially resolved velocity and velocity dispersion gradients are shown in Figs 3 and 4. Examples of model fits to the data are shown in Fig. 5. In all the spatially resolved profiles plotted here, the values of the parameters are plotted at the luminosity-weighted centres of the spatial bins used to derive the parameters. The spatially resolved kinematics was then used to fit spatially resolved, SSP-equivalent ages and metallicities (as presented in Tables 4–7). For the purpose of this study, the SFHs of the galaxies were analysed by fitting an SSP and composite stellar populations (CSPs) against the observed spectra of the galaxies. The errors given are the standard deviation (1σ) on the average values of the ages and [Fe/H] (where [Mg/Fe] = 0). These errors are determined by the MPFIT[5] algorithm which uses a covariance matrix to determine the best fit and the 1σ errors on the parameters (Koleva et al. 2009).

It is sometimes found that for a given galaxy, an SSP model cannot provide a satisfactory fit to the observed spectrum of the galaxy, implying that the galaxy experienced more than one star formation epoch and hence CSPs are used to represent the SFH. Each galaxy was fitted against three components (a young, intermediate and old component) and the optimal solutions were given in terms of the

[5] http://cow.physics.wisc.edu/~craigm/idl/idl.html

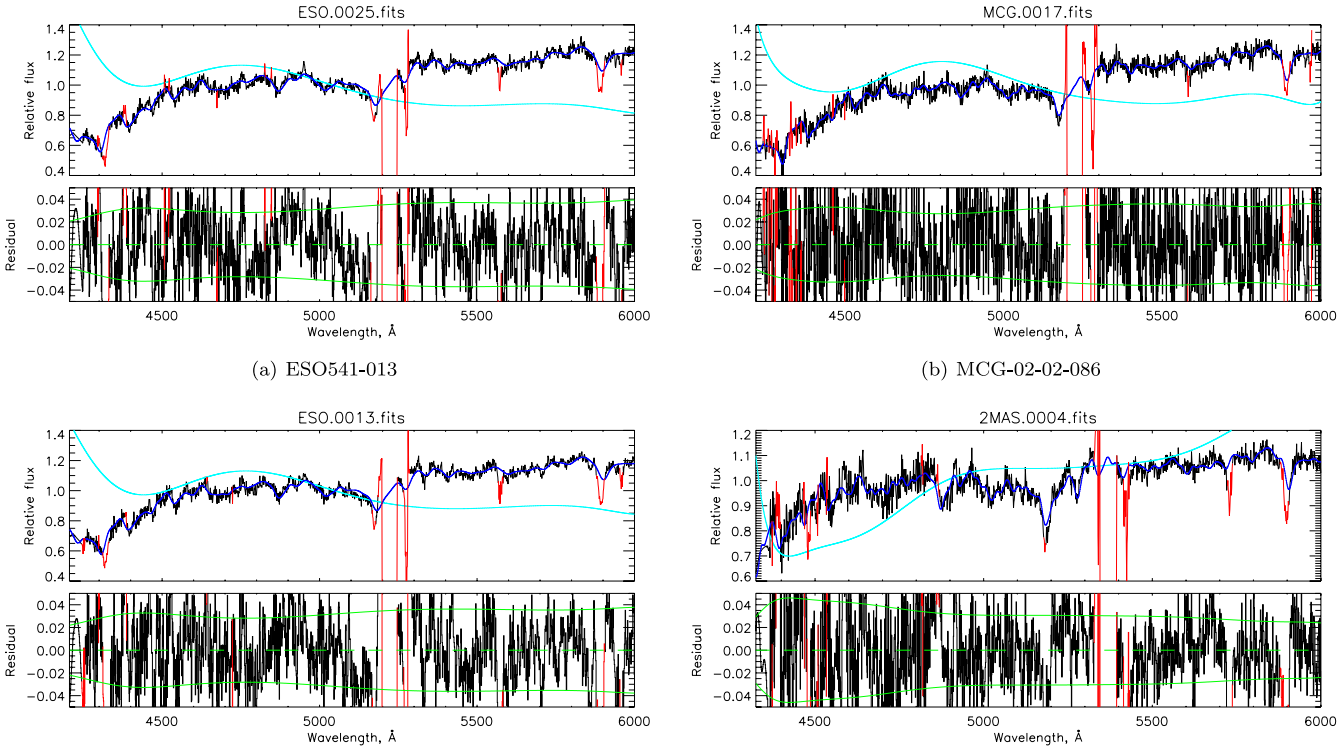

(a) ESO541-013 (b) MCG-02-02-086

(c) PGC023233 (d) 2MASXJ17122774-2322108

Figure 5. ULYSS fits to the central spectra of the four galaxies to derive the kinematics and stellar population properties. The red regions were masked in the fit.

Table 4. SSP-equivalent ages and metallicities fitted to 2MASX J17122774−2322108.

Radius (arcsec)	χ^2	Age (Myr)	[Fe/H]
−3.22	1.599	9796 ± 2714	− 0.556 ± 0.094
−1.70	1.544	4992 ± 808	− 0.032 ± 0.054
−0.94	1.032	4519 ± 744	0.082 ± 0.046
0.29	1.136	4196 ± 817	− 0.010 ± 0.054
0.64	0.087	5062 ± 829	− 0.059 ± 0.054
1.11	1.081	7178 ± 1316	− 0.171 ± 0.062
1.76	1.325	14 546 ± 3415	− 0.423 ± 0.076
3.22	2.202	9892 ± 2139	− 0.463 ± 0.076

age, [Fe/H], light fraction (LF), mass fraction (MF) and the errors on these values, following the procedure described below.

The time (age) axis can be divided into intervals by setting limits. For this paper three or less epochs were assumed: an older, an intermediate and a young stellar population. The three epochs were defined by setting limits on the ages (similar to the procedures in Bouchard et al. 2010; Du et al. 2010), while no limits were imposed on [Fe/H]. The age boundaries were (i) 12–20, (ii) 4–12 and (iii) 0.01–1.00 Gyr. Whenever CSP fits delivered results close to the boundaries of at least one of the three boxes, the upper or lower age boundaries of the boxes were changed until the results converged (in order not to artificially limit the three components to these chosen values – the three chosen intervals were just used as initial guesses). This method is also justified by the fact that whenever four or more components were fitted the weights of the additional components were zero. Thus there is no dependence of the young population mass fraction on any input parameter. Note that the oldest ages in these galaxies quite often hit the upper limits of the models, which are older than the current age of the Universe (see discussion in Sánchez-Blázquez et al. 2009). Therefore, all interpretations of these ages should be based on relative differences in ages which are much more reliable than absolute values. The results of the CSP fits are presented in Tables 8–11.

The constructed χ^2 maps are used to visualize the degeneracies between the parameters and to reveal the presence of the local minima. The χ^2 maps are based on a grid of initial guesses and a global minimization is then performed to evaluate the region where the parameter space converges to the absolute minimum of the χ^2 (Koleva et al. 2009). Figs 6–9 show the young (or only) stellar component derived for each of the four CCGs. The radial extent and percentage light fractions of the young stellar populations are shown in Fig. 10.

5 INDIVIDUAL GALAXIES

5.1 ESO 541−013 – Abell 0133

White et al. (1997) classified this cluster as a cooling-flow cluster, however, Bîrzan et al. (2004) and McCarthy et al. (2004) classified it as a non-cooling-flow cluster. More recently, McDonald et al. (2010) fit a null spectroscopic mass deposition rate to this cluster, whilst according to Hudson et al. (2010), Abell 0133 is a strong cool core cluster (based on the cooling time, which, in their analysis, seems to be the most robust indicator of the cool core strength). The classification of a host cluster as a cooling versus a non-cooling core is troublesome, so for our purposes we will just refer to this cluster as having a zero spectroscopically determined mass deposition rate without making further assumptions. The CCG showed extended

Table 5. SSP-equivalent ages and metallicities fitted to ESO 541−013.

Radius (arcsec)	χ^2	Age (Myr)	[Fe/H]
−9.24	1.901	3977 ± 837	0.282 ± 0.031
−7.25	1.294	13 700 ± 2345	−0.093 ± 0.056
−6.26	1.303	15 464 ± 2572	−0.179 ± 0.044
−5.62	1.219	12 303 ± 2091	0.006 ± 0.046
−5.15	1.220	5855 ± 427	0.197 ± 0.038
−4.80	1.289	13 543 ± 1962	−0.066 ± 0.049
−4.45	0.877	10 870 ± 1491	−0.009 ± 0.053
−3.92	0.999	16 376 ± 3123	0.086 ± 0.041
−3.69	1.090	6472 ± 267	0.166 ± 0.033
−3.45	0.929	5781 ± 509	0.154 ± 0.035
−3.22	0.926	6262 ± 369	0.120 ± 0.037
−3.00	0.829	12 895 ± 2072	0.044 ± 0.040
−2.75	0.799	10 347 ± 1656	−0.001 ± 0.046
−2.52	0.849	5794 ± 419	0.277 ± 0.036
−2.28	0.713	15 345 ± 2223	0.003 ± 0.038
−2.05	0.700	6198 ± 537	0.073 ± 0.035
−1.81	0.684	6196 ± 368	0.117 ± 0.036
−1.58	0.619	12 679 ± 1946	−0.043 ± 0.051
−1.40	0.647	15 853 ± 2568	0.012 ± 0.039
−1.29	0.835	11 246 ± 1676	0.015 ± 0.044
−1.17	0.799	12 359 ± 2019	0.010 ± 0.043
−1.05	0.604	14 442 ± 2255	−0.001 ± 0.040
−0.94	0.827	6047 ± 352	0.133 ± 0.035
−0.82	0.913	12 566 ± 2196	0.032 ± 0.042
−0.70	0.745	15 285 ± 2239	0.000 ± 0.040
−0.58	0.647	4072 ± 653	0.192 ± 0.026
−0.41	0.716	6395 ± 435	0.095 ± 0.035
−0.18	0.746	3487 ± 242	0.286 ± 0.046
0.00	0.624	6034 ± 268	0.192 ± 0.035
0.29	0.614	5961 ± 417	0.124 ± 0.036
0.53	0.612	6272 ± 247	0.180 ± 0.033
0.76	0.623	16 075 ± 2647	−0.001 ± 0.038
0.99	0.707	10 454 ± 1642	−0.001 ± 0.045
1.23	0.705	6007 ± 291	0.194 ± 0.035
1.46	0.749	13 429 ± 2121	−0.045 ± 0.053
1.70	0.844	15 986 ± 2738	−0.035 ± 0.048
1.93	0.846	15 614 ± 2544	0.015 ± 0.042
2.16	0.906	16 122 ± 2735	−0.007 ± 0.043
2.40	0.880	17 135 ± 3877	−0.002 ± 0.033
2.63	0.970	6361 ± 306	0.144 ± 0.035
2.87	0.975	11 949 ± 1628	−0.095 ± 0.054
3.10	0.968	15 958 ± 2818	0.023 ± 0.040
3.39	0.915	6057 ± 416	0.121 ± 0.038
3.74	0.929	20 000 ± 1000	0.001 ± 0.023
4.74	1.052	6160 ± 399	0.108 ± 0.036
5.62	1.110	11 960 ± 1875	−0.002 ± 0.047
7.20	1.381	11 110 ± 1831	−0.002 ± 0.054

Table 6. SSP-equivalent ages and metallicities fitted to MCG-02-02-086.

Radius (arcsec)	χ^2	Age (Myr)	[Fe/H]
−8.42	2.476	18 507 ± 2541	−0.226 ± 0.034
−6.20	2.368	20 000 ± 1000	−0.056 ± 0.025
−4.97	2.244	20 000 ± 1000	−0.123 ± 0.024
−4.16	2.173	20 000 ± 1000	−0.017 ± 0.025
−3.51	1.453	18 887 ± 4571	0.079 ± 0.030
−2.98	2.026	18 315 ± 2734	−0.046 ± 0.029
−2.57	1.974	20 000 ± 1000	−0.014 ± 0.025
−2.22	1.664	20 000 ± 1000	−0.027 ± 0.025
−1.87	1.470	19 261 ± 2173	−0.075 ± 0.027
−1.52	1.398	18 994 ± 2404	−0.072 ± 0.027
−1.17	1.307	20 000 ± 1000	0.047 ± 0.021
−0.88	1.615	20 000 ± 1000	−0.045 ± 0.024
−0.64	1.321	20 000 ± 1000	−0.010 ± 0.026
−0.41	1.315	20 000 ± 1000	−0.023 ± 0.025
−0.18	1.448	18 876 ± 2505	−0.088 ± 0.031
0.00	1.348	19 196 ± 1837	−0.115 ± 0.028
0.29	1.334	20 000 ± 1000	0.003 ± 0.021
0.47	1.991	20 000 ± 1000	−0.036 ± 0.025
0.64	1.425	18 638 ± 2786	−0.054 ± 0.032
0.88	1.288	20 000 ± 1000	−0.002 ± 0.021
1.11	1.168	20 000 ± 1000	−0.050 ± 0.025
1.35	1.399	17 074 ± 3735	−0.087 ± 0.030
1.58	1.176	17 165 ± 3930	−0.091 ± 0.031
1.87	1.144	14 961 ± 2016	−0.066 ± 0.046
2.22	1.118	16 172 ± 2802	−0.077 ± 0.040
2.63	1.213	16 288 ± 2747	−0.030 ± 0.040
3.10	0.913	18 197 ± 2738	−0.088 ± 0.035
3.57	0.950	13 814 ± 1870	−0.012 ± 0.044
4.04	1.048	20 000 ± 1000	−1.249 ± 0.022
4.50	1.201	20 000 ± 1000	0.001 ± 0.021
5.03	1.152	20 000 ± 1000	−0.017 ± 0.026
5.62	1.611	16 303 ± 2973	−0.005 ± 0.041
6.32	1.464	17 124 ± 3720	−0.076 ± 0.032
7.25	1.704	18 521 ± 2811	−0.069 ± 0.034
8.54	2.212	1780 ± 76	0.604 ± 0.020

Hα emission in McDonald et al. (2010). A single thin Hα filament (coincident with X-ray) extends north-east from the centre of the cluster for ∼25 kpc.

The χ^2 values of the SSP and CSP fits do not differ significantly, but the multiple component fitting was found to be more consistent (with the properties and number of components derived for the various spatial bins agreeing within the errors),[6] and showed that the majority of the bins consisted of two components: a large, very old component (bordering the upper limit of the stellar populations model at 20 Gyr), and a smaller very young component (<100 Myr) contributing up to ∼20 per cent of the light.

[6] We do not expect dramatic stellar population (in particular age) gradients for these galaxies, see Loubser & Sánchez-Blázquez (2012).

5.2 MCG-02-02-086 – Abell 0085

This CCG is hosted by a cooling flow cluster (see Table 1), but lacks a cD envelope (as summarized in Fisher, Illingworth & Franx 1995). It showed nuclear Hα emission in McDonald et al. (2010), and a large ring can be seen in the X-ray image (but without an Hα counterpart), resembling the outer edge of a bubble (McDonald et al. 2010). Based on the high Hα/NUV ratio, McDonald et al. (2010) postulated that the gas could be ionized by a recent burst of star formation in the CCG centre.

Similarly to ESO541-013, the χ^2 values of the SSP and CSP fits do not differ significantly, but the multiple component fitting was found to be more consistent. It showed that the majority of the bins consisted of two components, a large, very old component (bordering the upper limit of the stellar populations model at 20 Gyr), and a very small young component (of less than 1 Gyr contributing ∼ 5–10 per cent of the light). This agrees with the scenario (McDonald et al. 2010) postulated above.

Table 7. SSP-equivalent ages and metallicities fitted to PGC 023233.

Radius (arcsec)	χ^2	Age (Myr)	[Fe/H]
−4.09	2.992	14 650 ± 148	0.630 ± 0.022
−2.28	1.923	16 531 ± 2470	0.041 ± 0.032
−1.70	1.881	18 699 ± 2801	−0.036 ± 0.033
−1.23	1.691	16 146 ± 2447	0.025 ± 0.032
−0.94	1.509	16 245 ± 2687	0.127 ± 0.034
−0.41	1.056	12 700 ± 2248	0.124 ± 0.037
0.00	1.586	16 064 ± 2896	0.028 ± 0.031
0.41	1.002	13 529 ± 1795	0.013 ± 0.026
0.94	1.035	6790 ± 262	0.186 ± 0.027
1.23	1.200	11 453 ± 1272	−0.003 ± 0.031
1.46	1.381	6233 ± 226	0.140 ± 0.026
1.70	1.540	11 549 ± 1360	0.038 ± 0.030
1.87	1.370	6554 ± 202	0.167 ± 0.025
2.05	1.137	15 570 ± 1960	0.024 ± 0.026
2.28	1.120	7182 ± 651	0.130 ± 0.030
2.52	0.971	6437 ± 150	0.221 ± 0.027
2.75	0.959	16 001 ± 2306	0.057 ± 0.042
2.98	1.086	6469 ± 151	0.246 ± 0.035
3.39	1.249	14 610 ± 1839	−0.037 ± 0.029
3.74	2.152	9929 ± 1694	0.043 ± 0.033
4.09	2.281	20 000 ± 1000	−0.008 ± 0.038
4.45	2.713	15 995 ± 2588	0.090 ± 0.022
4.80	3.048	11 916 ± 907	0.548 ± 0.034
5.15	0.801	20 000 ± 1000	−0.002 ± 0.029
5.50	0.994	7284 ± 1408	0.040 ± 0.045
5.85	0.906	7385 ± 1560	0.055 ± 0.050

5.3 PGC 023233 – Abell 0644

This host cluster is classified as a cooling-flow cluster (see Table 1), and exhibited nuclear Hα emission in McDonald et al. (2010).

For this galaxy, the CSP fitting resulted in an inconsistent number of components (several bins consisting of one, two or three components – see Table 11), and the SSP fitting delivered an age estimate ranging between 6000 and 20 000 Myr (the upper limit of the model), with the majority of the bins being of intermediate age. Thus for this galaxy, it is difficult to accurately pinpoint the most probable age estimate and number of components.

It can be seen in fig. 6 in McDonald et al. (2010) that the upper limit of the global NUV luminosity of Abell 0644 (measured from archival *GALEX* images) lies barely above the star formation law (Kennicutt 1998). It is therefore not obviously younger or with more star formation activity than the other three galaxies analysed in this paper.

5.4 2MASX J17122774−2322108 – Ophiuchus

This low-density cluster was classified as a cooling-flow cluster (White et al. 1997), whereas McDonald et al. (2010) fit a null spectroscopic mass deposition rate to this cluster, The CCG showed nuclear Hα emission in McDonald et al. (2010).

Tables 4 and 8 show the SSP- and CSP-equivalent ages and metallicities derived for the galaxy. The χ^2 values of the SSP and CSP fits do not differ significantly, but once again the multiple component fitting was found to be more consistent, and showed that the majority of the bins consisted of a larger intermediate component of ∼7000 Myr and a smaller very young component of ∼10 Myr which contributes up to 25 per cent of the light.

5.5 Discussion

It is interesting to ask whether any particular distribution of star formation, and hence the young stars, can be detected in the observations. Fig. 10 shows the radial distribution of the young components. Only one galaxy (2MASX J17122774−2322108) shows a decrease in the fraction of the young stars as the radius increase from the centre of the galaxy. The other galaxies show that the young stars are equally present throughout the radius that our observations cover.

It is further necessary to take note of any possible AGN activity in the central galaxies, as the weak emission lines from AGN can fill in some of the absorption lines that is important for stellar population age measurements (such as the Balmer lines), and can ultimately lead to older derived age estimates. The total 1.4 GHz radio flux at the centre of a cluster may be indicative of AGN activity. For the four clusters we study here, we used the 1.4 GHz fluxes measured from the NRAO VLA Sky Survey (NVSS; Condon et al. 1998). All

Table 8. CSP ages and metallicities fitted to 2MASX J17122774−2322108.

Radius (arcsec)	χ^2	Number of components	Age (Myr)	[Fe/H]	Percentage light-weighted
−3.22	1.607	2	7159 ± 3505	0.232 ± 0.171	50.0
			12 911 ± 17 844	−2.037 ± 0.257	50.0
−1.70	1.519	2	16 ± 14	−1.234 ± 1.499	23.0
			7165 ± 2367	0.162 ± 0.059	77.0
−0.94	1.040	2	10 ± 100	−2.100 ± 0.915	21.5
			7139 ± 1835	0.213 ± 0.052	78.5
0.29	1.106	2	10 ± 100	−2.301 ± 1.000	24.4
			7170 ± 1913	0.164 ± 0.056	75.6
0.64	0.826	2	13 ± 8	−2.034 ± 0.983	26.1
			7225 ± 4191	0.198 ± 0.181	74.1
1.11	1.085	3	16 ± 24	−0.995 ± 1.851	7.9
			7178 ± 2774	0.165 ± 0.088	70.6
			20 000 ± 2000	−2.301 ± 1.000	21.4
1.76	1.325	1	14 546 ± 3415	−0.423 ± 0.076	100.0
3.22	2.202	1	9892 ± 2139	−0.463 ± 0.076	100.0

Table 9. CSP ages and metallicities fitted to ESO 541−013.

Radius (arcsec)	χ^2	Number of components	Age (Myr)	[Fe/H]	Percentage light-weighted
−9.24	1.753	2	1665 ± 2918	−2.291 ± 1.238	11.0
			18 375 ± 6844	0.118 ± 0.047	89.0
−7.25	1.245	2	86 ± 66	−2.301 ± 1.000	16.4
			20 000 ± 1000	0.079 ± 0.037	83.6
−6.26	1.280	2	10 ± 10	−1.933 ± 1.817	15.3
			20 000 ± 1000	−0.009 ± 0.041	84.7
−5.62	1.158	2	46 ± 50	−2.301 ± 1.000	13.6
			19 075 ± 1056	0.117 ± 0.045	86.4
−5.15	1.213	2	4192 ± 2515	−1.642 ± 1.084	31.9
			20 000 ± 1000	0.640 ± 0.043	68.1
−4.80	1.172	2	10 ± 10	−1.826 ± 0.993	16.4
			20 000 ± 1000	0.092 ± 0.035	83.6
−4.45	0.892	2	12 ± 14	−1.707 ± 1.537	17.0
			20 000 ± 1000	0.013 ± 0.110	83.0
−3.92	1.010	2	25 ± 21	−2.301 ± 1.000	17.5
			17 850 ± 2950	0.216 ± 0.045	82.5
−3.69	0.892	2	12 ± 9	−1.893 ± 0.895	13.5
			20 000 ± 1000	0.027 ± 0.088	86.5
−3.45	0.772	2	23 ± 16	−2.301 ± 1.000	19.0
			17 967 ± 2672	0.295 ± 0.047	81.0
−3.22	0.836	2	10 ± 10	−1.875 ± 1.511	16.6
			18 337 ± 5915	0.162 ± 0.050	83.4
−3.00	0.789	2	271 ± 364	−2.301 ± 1.000	9.0
			17 920 ± 7133	0.139 ± 0.477	91.0
−2.75	0.656	2	23 ± 13	−2.301 ± 1.000	18.2
			20 000 ± 1000	0.024 ± 0.066	81.8
−2.52	0.752	2	10 ± 10	−1.926 ± 1.455	18.5
			18 224 ± 2983	0.291 ± 0.050	81.5
−2.28	0.639	2	10 ± 10	−1.912 ± 1.048	18.5
			20 000 ± 1000	0.085 ± 0.059	81.5
−2.05	0.616	2	25 ± 18	−2.301 ± 1.000	16.9
			18 238 ± 5483	0.161 ± 0.040	83.1
−1.81	0.604	2	10 ± 10	−1.938 ± 1.471	18.8
			18 604 ± 6650	0.153 ± 0.047	81.2
−1.58	0.615	2	14 ± 22	−1.619 ± 2.739	12.9
			20 000 ± 1000	0.039 ± 0.100	87.1
−1.40	0.595	2	11 ± 9	−1.804 ± 2.716	14.2
			19 201 ± 7353	0.150 ± 0.064	85.8
−1.29	0.813	2	294 ± 176	−2.301 ± 1.000	12.6
			18 376 ± 7278	0.164 ± 0.064	87.4
−1.17	0.712	2	26 ± 17	−2.301 ± 1.000	17.4
			18 060 ± 3925	0.214 ± 0.043	82.6
−1.05	0.586	2	1039 ± 879	−2.301 ± 1.000	8.7
			17 848 ± 4294	0.106 ± 0.071	91.3
−0.94	0.763	2	10 ± 10	−1.918 ± 1.270	21.0
			18 362 ± 4096	1.270 ± 0.231	79.0
−0.82	0.896	2	10 ± 10	−0.408 ± 0.338	19.5
			17 839 ± 2230	0.279 ± 0.054	80.5
−0.70	0.692	2	10 ± 10	−1.923 ± 1.777	15.0
			18 323 ± 4399	0.200 ± 0.044	85.0
−0.58	0.567	2	26 ± 23	−2.301 ± 1.000	13.6
			20 000 ± 1000	0.075 ± 0.068	82.4
−0.41	0.643	2	30 ± 29	−2.301 ± 1.000	12.2
			20 000 ± 1000	0.081 ± 0.033	87.8
−0.18	0.697	2	97 ± 72	−1.382 ± 1.153	16.3
			18 279 ± 9589	0.150 ± 0.110	83.7
0.00	0.542	2	27 ± 17	−2.301 ± 1.000	13.9
			20 000 ± 1000	0.053 ± 0.095	86.1
0.29	0.495	2	28 ± 19	−2.301 ± 1.000	15.2
			20 000 ± 1000	−0.005 ± 0.151	84.8
0.53	0.525	2	27 ± 15	−2.301 ± 1.000	19.3
			17 945 ± 3333	0.223 ± 0.045	80.7

Table 9 – *continued*

Radius (arcsec)	χ^2	Number of components	Age (Myr)	[Fe/H]	Percentage light-weighted
0.76	0.504	2	10 ± 10	−1.936 ± 0.695	16.5
			20 000 ± 1000	−0.001 ± 0.118	83.5
0.99	0.683	2	25 ± 17	−2.301 ± 1.000	17.0
			18 954 ± 5435	1.149 ± 0.040	83.0
1.23	0.601	3	45 ± 43	−2.301 ± 1.000	12.9
			9517 ± 8060	−0.259 ± 1.047	20.9
			18 895 ± 4275	0.577 ± 0.079	66.1
1.46	0.709	2	27 ± 25	−2.301 ± 1.000	11.9
			20 000 ± 1000	0.036 ± 0.033	88.1
1.70	0.780	2	26 ± 20	−2.301 ± 1.000	15.3
			20 000 ± 1000	0.067 ± 0.034	84.7
1.93	0.834	2	946 ± 2782	−1.548 ± 3.877	9.6
			18 656 ± 4024	0.205 ± 0.072	90.4
2.16	0.891	2	13 ± 10	−1.677 ± 1.528	14.7
			20 000 ± 8730	0.051 ± 0.056	85.3
2.40	0.912	2	10 ± 10	0.699 ± 1.000	23.4
			19 908 ± 3166	0.214 ± 0.042	76.6
2.63	0.853	2	27 ± 17	−2.301 ± 1.000	14.7
			20 000 ± 1000	0.050 ± 0.084	83.3
2.87	0.857	2	10 ± 10	−2.301 ± 1.000	30.1
			18 783 ± 4473	0.246 ± 0.071	69.9
3.10	0.967	2	434 ± 733	−2.301 ± 1.000	13.3
			18 102 ± 4852	0.185 ± 0.039	86.7
3.39	0.934	2	48 ± 58	−2.301 ± 1.000	12.7
			20 000 ± 1000	0.075 ± 0.062	87.3
3.74	0.913	2	24 ± 25	−2.301 ± 1.000	13.5
			19 353 ± 1163	0.111 ± 0.101	86.5
4.74	1.032	2	39 ± 34	−2.301 ± 1.000	12.2
			20 000 ± 1000	0.105 ± 0.032	87.8
5.62	1.037	2	10 ± 10	−2.085 ± 1.117	22.1
			20 000 ± 1000	0.113 ± 0.061	78.9
7.20	1.113	2	179 ± 230	−2.301 ± 1.000	14.2
			19 464 ± 1287	0.097 ± 0.055	85.8

but one galaxy (PGC 023233) show radio emission in Figs A1–A4. The Hα filaments measured in McDonald et al. (2010) are very small (<4 kpc) in comparison with the extensive radio emission, but are located in the centres of the 1.4 GHz and X-ray emission.

Previous optical emission-line and ultraviolet studies can then be included to quantitatively determine whether AGN contamination is present in the optical spectra. Three of the four galaxies (all except ESO 541−013) have nuclear Hα emission. ESO 541−013 is classified as a non-emission line galaxy by Edwards et al. (2007), as its Hβ equivalent width is -0.08 ± 0.09 Å (after correcting for the underlying absorption), whereas emission galaxies are classified with Hβ equivalent width as >0.5 Å. Using this same criteria, MCG-02-02-086 is classified as a galaxy with star-forming activity as its Hβ equivalent width is 1.13 ± 0.21 Å (and no AGN activity is suspected). From the *GALEX* NUV excess, Hicks, Mushotzky & Donahue (2010) estimate a star formation rate of 0.004 $M_\odot$ yr^{-1} (assuming continuous star formation over 20 Myr) for PGC 023233 (with no evidence of AGN activity). 2MASX J17122774−2322108, however, is a suspected AGN (see Perez-Torres et al. 2009; Murgia et al. 2010). It therefore seems that for three of the four galaxies, no AGN are hosted but weak star formation for MCG-02-02-086 and PGC 023233 are confirmed by previous observations. No emission features were found within our slit positions for all four galaxies.

No significant stellar population gradients are measured along the major axis, which are mostly aligned with the radio emission (Fig. 1 compared to Figs A1–A4). As discussed in Loubser & Sánchez-Blázquez (2012), because the models predict that the majority of mergers happen at recent times, the gas content of the accreted galaxies is believed to be low (e.g. Dubinski 1998; Conroy, Wechsler & Kravtsov 2007; De Lucia & Blaizot 2007) and these mergers would therefore not change the central ages and metallicities of the CCGs. This would explain the lack of large differences between the stellar populations of CCGs and normal galaxies. However, these merger or accretion events are expected to change stellar population gradients, as dry minor mergers would deposit metal poor stars outwards (Kawata et al. 2006). Thus, metallicity gradients in galaxies affected by mergers would be steeper than their non-merger counterparts. We can therefore not deduce any merger events from these observations which were centred on the nucleus of these extended galaxies.

6 CONCLUSION

We have obtained, analysed and interpreted detailed, high spatial and spectral resolution, long-slit observations of four CCGs (Abell 0085, 0133, 0644 and Ophiuchus) recently obtained on SALT, to probe the spatially resolved kinematics and stellar populations of the stars. We use the PEGASE.HR model with the ELODIE v3.1 stellar library to determine the SFHs of the galaxies using the

Table 10. CSP ages and metallicities fitted to MCG-02-02-086.

Radius (arcsec)	χ^2	Number of components	Age (Myr)	[Fe/H]	Percentage light-weighted
−8.42	2.430	2	433 ± 1169	−0.426 ± 2.046	10.2
			19 998 ± 2412	−0.139 ± 0.102	89.8
−6.20	2.343	2	422 ± 1636	−0.143 ± 3.123	6.4
			20 000 ± 1000	−0.011 ± 0.063	93.6
−4.97	2.197	1	20 000 ± 1000	−0.129 ± 0.024	100.0
−4.16	2.132	2	10 ± 100	0.699 ± 0.100	14.5
			20 000 ± 1000	0.055 ± 0.032	85.5
−3.51	1.477	2	984 ± 1172	−2.301 ± 0.100	5.6
			18 588 ± 5136	0.142 ± 0.036	94.4
−2.98	1.927	2	421 ± 760	−0.356 ± 1.533	10.9
			20 000 ± 1000	0.043 ± 0.055	89.1
−2.57	1.848	2	10 ± 100	0.699 ± 0.100	19.5
			18 715 ± 6040	0.138 ± 0.040	80.5
−2.22	1.633	2	364 ± 963	−2.301 ± 0.100	6.7
			20 000 ± 1000	0.010 ± 0.026	93.7
−1.87	1.483	2	689 ± 4658	−0.469 ± 0.874	3.8
			20 000 ± 1000	−0.031 ± 0.076	96.2
−1.52	1.398	2	1018 ± 838	−2.301 ± 0.100	7.6
			20 000 ± 1000	0.001 ± 0.042	92.4
−1.17	1.320	2	314 ± 1299	−2.298 ± 0.926	5.3
			18 967 ± 7059	0.109 ± 0.041	94.7
−0.88	1.602	1	20 000 ± 1000	−0.034 ± 0.046	100.0
−0.64	1.311	1	20 000 ± 1000	−0.004 ± 0.035	100.0
−0.41	1.316	1	20 000 ± 1000	−0.031 ± 0.031	100.0
−0.18	1.433	2	693 ± 5963	−0.701 ± 0.226	3.4
			20 000 ± 1000	−0.047 ± 0.087	96.6
0.00	1.350	2	544 ± 6806	−1.378 ± 0.720	1.6
			19 740 ± 3117	−0.088 ± 0.081	98.4
0.29	1.362	2	603 ± 2830	−2.301 ± 0.100	4.6
			20 000 ± 1000	0.037 ± 0.041	95.4
0.47	2.000	2	30 ± 83	0.699 ± 0.100	4.4
			20 000 ± 1000	−0.006 ± 0.030	95.6
0.64	1.424	2	857 ± 2060	−2.301 ± 0.100	5.4
			20 000 ± 1000	−0.001 ± 0.030	94.6
0.88	1.294	2	447 ± 1864	−1.198 ± 0.883	4.4
			20 000 ± 1000	0.039 ± 0.050	95.6
1.11	1.197	2	693 ± 1951	−1.667 ± 0.578	4.7
			20 000 ± 1000	−0.008 ± 0.062	95.3
1.35	1.322	2	1056 ± 605	−2.301 ± 0.100	11.3
			20 000 ± 1000	0.036 ± 0.058	88.7
1.58	1.186	2	969 ± 576	−2.301 ± 0.100	9.3
			20 000 ± 1000	0.000 ± 0.028	90.7
1.87	1.058	2	45 ± 40	0.571 ± 0.671	13.0
			20 000 ± 1000	0.037 ± 0.034	87.0
2.22	1.059	2	10 ± 100	0.699 ± 0.100	18.0
			20 000 ± 1000	0.088 ± 0.035	82.0
2.63	1.146	2	97 ± 236	−1.707 ± 0.300	7.3
			20 000 ± 1000	0.027 ± 0.030	92.7
3.10	0.899	2	1101 ± 1416	−2.301 ± 0.100	6.1
			20 000 ± 1000	−0.014 ± 0.078	93.9
3.57	0.895	2	83 ± 75	−2.301 ± 0.100	11.1
			17 901 ± 4854	0.095 ± 0.037	88.9
4.04	1.064	2	170 ± 530	−0.895 ± 0.363	6.9
			20 000 ± 1000	0.079 ± 0.034	93.1
4.50	1.197	2	547 ± 1064	−1.603 ± 0.239	6.7
			18 771 ± 6648	0.912 ± 0.079	93.3
5.03	1.166	2	508 ± 852	−1.691 ± 0.347	6.2
			20 000 ± 1000	0.014 ± 0.063	93.8
5.62	1.546	2	87 ± 78	−2.301 ± 0.100	15.3
			19 034 ± 8377	0.123 ± 0.050	84.7
6.32	1.425	2	953 ± 667	−2.301 ± 0.100	7.4
			20 000 ± 1000	0.006 ± 0.027	92.6
7.25	1.644	2	409 ± 675	−0.338 ± 1.463	12.7
			20 000 ± 1000	0.018 ± 0.058	87.3
8.54	2.105	2	54 ± 26	0.632 ± 0.295	24.8
			18 777 ± 3812	0.214 ± 0.048	75.2

Table 11. CSP ages and metallicities fitted to PGC 023233.

Radius (arcsec)	χ^2	Number of components	Age (Myr)	[Fe/H]	Percentage light-weighted
−4.09	2.887	1	15 000 ± 2013	0.565 ± 0.056	100
−2.28	1.969	3	1996 ± 3534	− 2.225 ± 1.795	5.1
			15 657 ± 11 466	− 0.261 ± 0.263	48.2
			18 985 ± 4827	0.699 ± 0.100	46.7
−1.70	1.863	1	18 906 ± 3604	− 0.016 ± 0.046	100.0
−1.23	1.716	3	15 ± 38	− 2.293 ± 2.603	2.4
			5553 ± 597	0.699 ± 0.100	31.5
			15 237 ± 5014	− 0.344 ± 0.117	66.1
−0.94	1.524	2	3490 ± 3572	− 2.138 ± 0.932	10.8
			17 728 ± 1798	0.225 ± 0.057	89.2
−0.41	1.035	2	13 289 ± 1994	0.604 ± 0.186	30.6
			17 447 ± 7607	− 0.010 ± 0.232	69.4
0.00	1.681	3	1457 ± 1173	− 2.301 ± 0.897	4.9
			5566 ± 907	0.616 ± 0.057	36.8
			20 000 ± 1000	− 0.456 ± 0.194	58.3
0.41	0.994	1	16 445 ± 6298	0.160 ± 0.126	100
0.94	1.032	2	15 409 ± 764	0.699 ± 0.100	53.5
			18 724 ± 6200	− 0.304 ± 0.138	46.5
1.23	1.164	1	17 845 ± 1652	0.222 ± 0.059	100
1.46	1.324	2	15 485 ± 3385	0.435 ± 0.073	70.9
			20 000 ± 2851	− 1.221 ± 0.540	29.1
1.70	1.449	3	1125 ± 2532	− 1.261 ± 2.593	3.1
			10 937 ± 10 483	0.308 ± 0.251	44.5
			14 581 ± 15 333	− 0.410 ± 0.475	52.4
1.87	1.340	2	2000 ± 1000	− 2.301 ± 0.100	7.9
			16 699 ± 4022	0.142 ± 0.034	92.1
2.05	1.126	2	1043 ± 1091	− 1.202 ± 2.232	5.4
			19 782 ± 3813	− 0.112 ± 0.192	94.6
2.28	1.068	3	164 ± 119	0.699 ± 0.100	3.9
			17 753 ± 3748	0.664 ± 0.071	39.0
			20 000 ± 1000	− 0.178 ± 0.163	57.0
2.52	0.913	3	287 ± 397	− 2.301 ± 0.100	6.0
			4559 ± 5052	0.697 ± 0.625	1.0
			16 689 ± 6653	0.133 ± 0.069	93.0
2.75	0.964	3	13 ± 22	0.504 ± 0.802	8.8
			15 355 ± 3355	0.660 ± 0.451	25.0
			17 119 ± 7186	0.056 ± 0.351	65.2
2.98	1.058	2	6962 ± 8416	− 2.240 ± 0.568	14.8
			14 028 ± 2916	0.315 ± 0.067	85.2
3.39	1.240	2	10 ± 100	0.588 ± 0.616	6.9
			17 568 ± 4033	0.005 ± 0.054	93.1
3.74	2.110	3	139 ± 2036	− 2.291 ± 1.497	1.0
			9180 ± 6168	− 2.187 ± 0.371	26.8
			16 273 ± 5440	0.446 ± 0.067	72.2
4.09	2.244	3	203 ± 6561	− 1.161 ± 2.579	0.5
			11 888 ± 13 042	− 0.818 ± 0.428	40.5
			18 810 ± 4744	0.632 ± 0.0060	59.0
4.45	2.800	2	508 ± 2003	− 0.464 ± 2.551	6.5
			16 109 ± 3997	− 0.145 ± 0.077	93.5
4.80	3.048	1	11 916 ± 907	0.548 ± 0.034	100.0
5.15	0.801	1	20 000 ± 1000	− 0.002 ± 0.029	100.0
5.50	0.994	1	7284 ± 1408	0.040 ± 0.045	100.0
5.85	0.906	1	7385 ± 1560	0.055 ± 0.050	100.0

full spectrum fitting. We perform SSP as well as CSP fits to account for more complex SFHs. Monte Carlo simulations and χ^2 maps are used to check the reliability of the solutions. We emphasize that we only interpret the presence of young stellar components which is much more reliable than interpreting the absolute ages, metallicities and α enhancements.

Hudson et al. (2010) use the largest complete sample of 64 galaxy clusters (Highest X-ray Flux Galaxy Cluster Sample) with available high-quality X-ray data from *Chandra*, and apply 16 cool-core diagnostics to them. To segregate cool-core and non-cool-core clusters, they find that central cooling time is the best parameter for low-redshift clusters with high-quality data. They further show that the

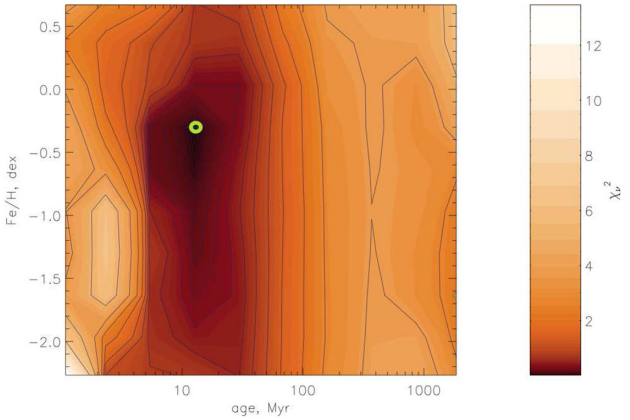

Figure 6. χ^2 map of the young component of ESO 541−013. The global minimum is indicated with a green circle.

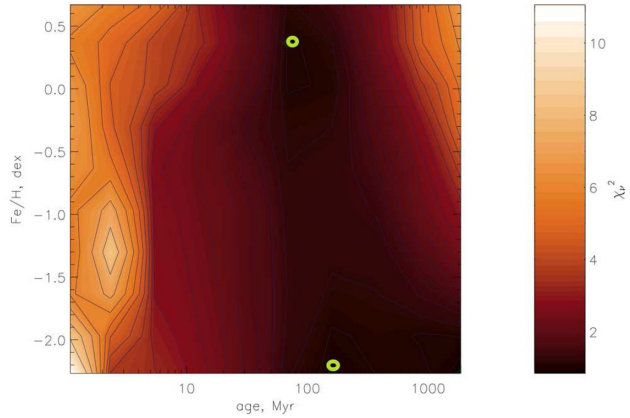

Figure 7. χ^2 map of the young component of MCG-02-02-086. The global minimum can be seen as a green circle at the bottom (right-hand corner) of the map, and the next probable solution is also shown at the top (middle) of the map.

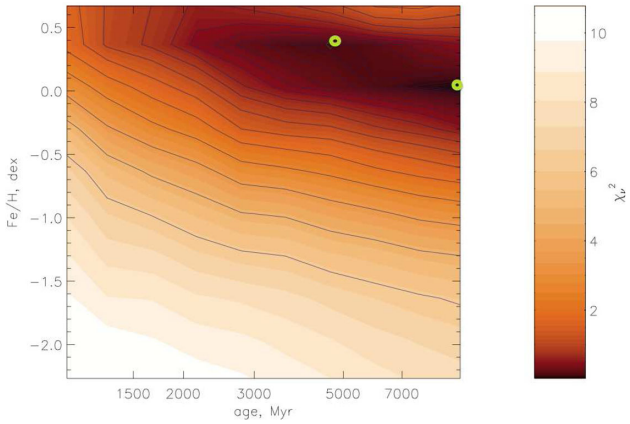

Figure 8. χ^2 map of the only component of PGC 023233 (SSP is the best fit). The global minimum can be seen as a green circle at the right of the map, with the second most probable solution to the left.

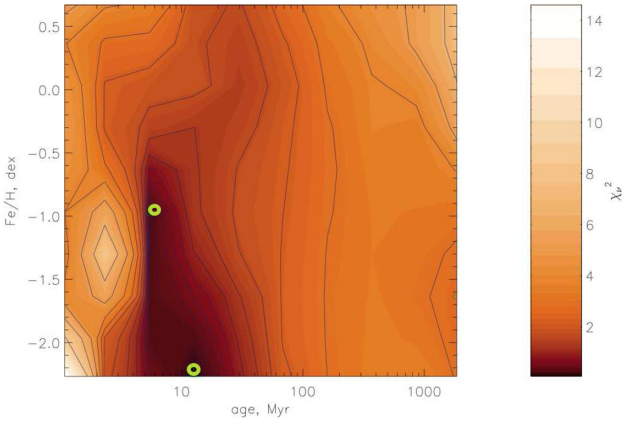

Figure 9. χ^2 map of the young component in the centre of 2MASX J17122774−2322108. The global minimum can be seen as a green circle at the bottom of the map, with the second most probable solution above.

discrepancy in classical and spectroscopic mass deposition rates cannot be explained with a recent formation of the cool cores, demonstrating the need for a heating mechanism to explain the cooling flow problem.

Only a few CCGs have been reported in the literature with ongoing or recent bursts of star formation, and the majority – if not all of them – are hosted in 'cooling flow' clusters. Rafferty et al. (2008), Cavagnolo et al. (2008, 2009) and Hoffer et al. (2012) show that central galaxies in clusters with low entropy (K_0) – thus with large cooling rates – are the only CCGs to exhibit signs of vigorous star formation. Here, we detect very small, but observable young stellar components in two of our four clusters which have no mass deposition rates (or very little so that it is below the X-ray detection limit). This suggests another possible mechanism for the recent star formation such as galactic cannibalism that appears in cluster environments due to dynamical friction. We note that the spatially resolved recession velocity of these two galaxies (2MASX J17122774−2322108 and ESO 541−013) show measurable rotation (see Fig. 3), although the sample is too small to infer a possible difference between the kinematics of these galaxies and the galaxy with a younger component hosted by a cooling flow cluster. Abell 0133 (host of ESO 541−013) showed extended H-α filaments in McDonald et al. (2010), whereas the other three clusters examined here showed nuclear H-α emission. Therefore no obvious correlation between the H-α gas and stellar kinematics exists. Mergers that are not dissipationless can supply fresh cold gas that can trigger an episode of star formation (Mihos & Hernquist 1996). A large library of smooth particle hydrodynamic simulations of galaxy mergers (Di Matteo et al. 2007, 2008) show that the average enhancement of the star formation rate in a random galaxy collision is only a factor of a few (3–4 being the median factor) and only lasts 200–400 Myr. This process is more efficient in dense clusters but the star formation rate increase remains in general below a factor of 10 or less (Martig & Bournaud 2008).

Since we have carefully measured the possible presence of emission lines (with particular attention to the Balmer lines), and could not find any detections above 3σ of the noise of the spectra in any of the four objects – we conclude that our slit placement did not

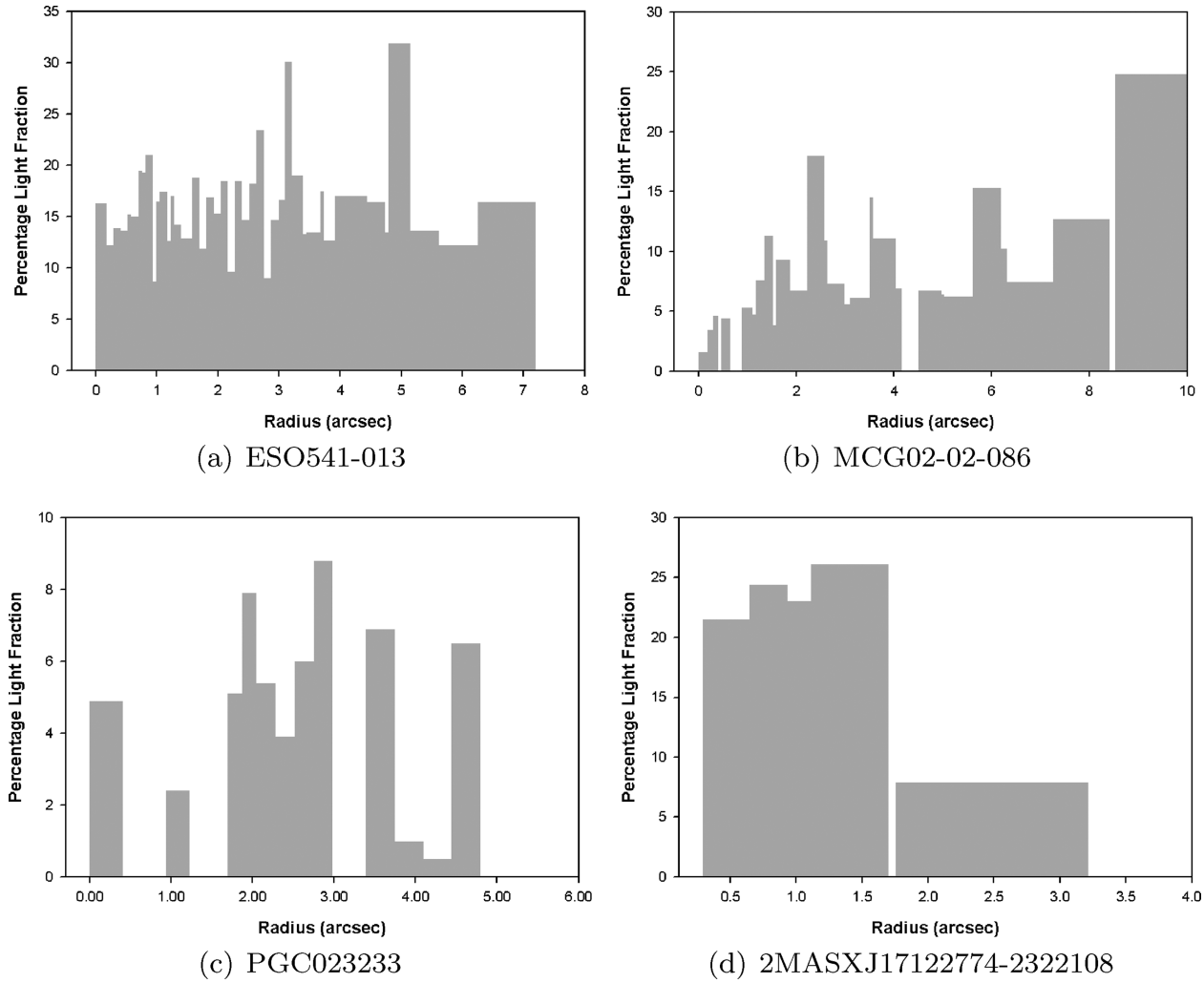

Figure 10. The radial extent and percentage light fractions of the young stellar populations.

intercept the Hα filaments. Thus in our data, the relatively young stars do not necessarily co-exist with the Hα emitting gas.

This study, focusing on the detailed analysis of four objects, is complementary to our previous studies investigating the evolution and environmental influence in a larger sample of CCGs (Loubser et al. 2008; Loubser & Sánchez-Blázquez 2012). Throughout the investigation and analysis of the larger sample, a picture emerged indicating that the kinematics and stellar population properties of the central galaxies are not very dependent on the galaxy mass (with the exception of the metallicity gradients which are dependent on the galaxy velocity dispersions). Similarly, various cluster properties also seem to have very limited influence on the central galaxy stellar population properties, such as cluster temperature or density. On the other hand, the offset between the X-ray peak of the cluster and the galaxy and the cooling flows in the clusters do influence the probability that the central galaxy will form stars. In Loubser et al. (2008), we found that one of the six younger galaxies was hosted by a non-cooling flow cluster whereas the other five younger galaxies were hosted by a cooling-flow cluster. This previous study analysed only the SSP-equivalent ages, but reinforces the findings of the current study. All of these observations point to very diverse SFHs of these central galaxies, and excludes the naive picture of very passive, homogeneous evolution.

ACKNOWLEDGEMENTS

SIL is financially supported by the South African National Research Foundation. SIL gratefully acknowledges the constructive comments from the anonymous reviewer as well as the help of Alet de Witt (Hartebeesthoek Radio Observatory) with the radio data interpretation. All of the observations reported in this paper were obtained with the Southern African Large Telescope (SALT) under program 2011-2-RSA_OTH-003 and 2012-1-RSA_OTH-003 (PI: Ilani Loubser).

REFERENCES

Bertelli G., Bressan A., Chiosi C., Fagotto F., Nasi E., 1994, A&AS, 106, 275
Bildfell C., Hoekstra H., Babul A., Mahdavi A., 2008, MNRAS, 389, 1637
Bîrzan L., Rafferty D. A., McNamara B. R., Wise M. W., Nulsen P. E. J., 2004, ApJ, 607, 800
Bouchard A., Prugniel P., Koleva M., Sharina M., 2010, A&A, 513, A45
Burgh E. B., Nordsieck K. H., Kobulnicky H. A., Williams T. B., O'Donoghue D., Smith M. P., Percival J. W., 2003, Proc. SPIE, 4841, 1463
Cappellari M., Emsellem E., 2004, PASP, 116, 138
Cardiel N., Gorgas J., Aragón-Salamanca A., 1998, MNRAS, 298, 977

Cavagnolo K. W., Donahue M., Voit G. M., Sun M., 2008, ApJ, 683, 107
Cavagnolo K. W., Donahue M., Voit G. M., Sun M., 2009, ApJS, 182, 12
Condon J. J., Cotton W. D., Greissen E. W., Yin Q. F., Perley R. A., Taylor G. B., Broderick J. J., 1998, AJ, 115, 1693
Conroy C., Wechsler R. H., Kravtsov A. V., 2007, ApJ, 668, 826
Crawford C. S., Allen S. W., Ebeling H., Edge A. C., Fabian A. C., 1999, MNRAS, 306, 857
Crawford S. M. et al., 2010, Proc. SPIE, 7737E, 54
De Lucia G., Blaizot J., 2007, MNRAS, 375, 2
Di Matteo P., Combes F., Melchior A.-L., Semelin B., 2007, A&A, 468, 61
Di Matteo P., Bournaud F., Martig M., Combes F., Melchior A.-L., Semelin B., 2008, A&A, 492, 31
Du W., Luo A. L., Prugniel Ph., Liang Y. C., Zhao Y. H., 2010, MNRAS, 409, 567
Dubinski J., 1998, ApJ, 502, 141
Edwards L. O. V., Hudson M. J., Balogh M. L., Smith R. J., 2007, MNRAS, 379, 100
Fisher D., Illingworth G., Franx M., 1995, ApJ, 438, 539
Hicks A. K., Mushotzky R., Donahue M., 2010, ApJ, 719, 1844
Hoffer A. S., Donahue M., Hicks A., Barthelemy R. S., 2012, ApJS, 199, 23
Hudson D. S., Mittal R., Reiprich T. H., Nulsen P. E. J., Andernach H., Sarazin C. L., 2010, A&A, 513, 37
Jarrett T. H., Chester T., Cutri R., Schneider S. E., Huchra J. P., 2003, AJ, 125, 525
Kawata D., Mulchaey J. S., Gibson B. K., Sánchez-Blázquez P., 2006, ApJ, 648, 969
Kennicutt R. C., 1998, ApJ, 498, 541
Kobulnicky H. A., Nordsieck K. H., Burgh E. B., Smith M. P., Percival J. W., Williams T. B., O'Donoghue D., 2003, Proc. SPIE, 4841, 1634
Koleva M., Prugniel Ph., Ocvirk P., Le Borgne D., Soubiran C., 2008, MNRAS, 385, 1998
Koleva M., Prugniel Ph., Bouchard A., Wu Y., 2009, A&A, 501, 1269
Liu F. S., Mao S., Meng X. M., 2012, MNRAS, 423, 422
Loubser S. I., Sánchez-Blázquez P., 2012, MNRAS, 425, 841
Loubser S. I., Soechting I. K., 2013, MNRAS, 431, 2933
Loubser S. I., Sansom A. E., Sánchez-Blázquez P., Soechting I. K., Bromage G., 2008, MNRAS, 391, 1009
Loubser S. I., Sánchez-Blázquez P., Sansom A. E., Soechting I. K., 2009, MNRAS, 398, 133
McCarthy I. G., Balogh M. L., Babul A., Poole G. B., Horner D. J., 2004, ApJ, 613, 811
McDonald M., Veilleux S., Rupke D. S. N., Mushotzky R., 2010, ApJ, 721, 1262
McDonald M., Veilleux S., Rupke D. S. N., 2012, ApJ, 746, 153
McNamara B. R. et al., 2006, ApJ, 648, 164
Martig M., Bournaud F., 2008, MNRAS, 385, L38
Mihos J., Hernquist L., 1996, ApJ, 464, 641
Murgia M., Eckert D., Govoni F., Ferrari C., Pandey-Pommier M., Nevalainen J., Paltani S., 2010, A&A, 514, 76
O'Dea C. P. et al., 2008, ApJ, 681, 1035
O'Dea K. P. et al., 2010, ApJ, 719, 1619
Perez-Torres M. A., Zandanel F., Guerrero M. A., Pal S., Profumo S., Prada F., Panessa F., 2009, MNRAS, 396, 2237
Pipino A., Kaviraj S., Bildfell C., Hoekstra H., Babul A., Silk J., 2009, MNRAS, 395, 462
Prugniel Ph., Soubiran C., Koleva M., Le Borgne D., 2007, preprint (astro-ph/0703658)
Rafferty D. A., McNamara B. R., Nulsen P. E. J., 2008, ApJ, 687, 899
Salpeter E. E., 1955, ApJ, 121, 161
Sánchez-Blázquez P. et al., 2006, MNRAS, 371, 703
Sánchez-Blázquez P. et al., 2009, A&A, 499, 47
Sarzi M. et al., 2006, MNRAS, 366, 1151
van Dokkum P. G., 2001, PASP, 113, 1420
Viljoen D., Loubser S. I., 2013, MNRAS, submitted
Voigt L. M., Fabian A. C., 2004, MNRAS, 347, 1130
Voit G. M., Cavagnolo K. W., Donahue M., Rafferty D. A., McNamara B. R., Nulsen P. E. J., 2008, ApJ, 681, 5
White D. A., Jones C., Forman W., 1997, MNRAS, 292, 419

APPENDIX A: STELLAR KINEMATICS

The spatially resolved kinematic data for all four CCGs are available as online data.

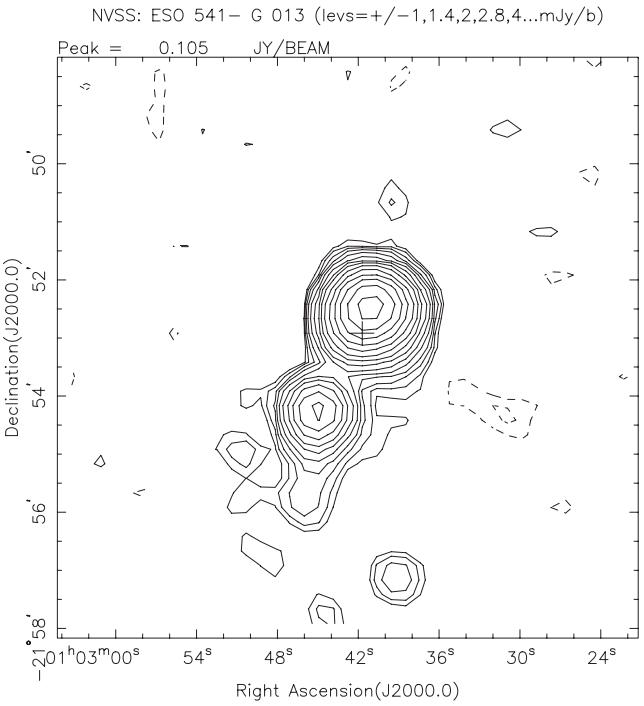

Figure A1. ESO 541−013 NRAO VLA Sky Survey (NVSS) 10 × 10 arcmin^2 image.

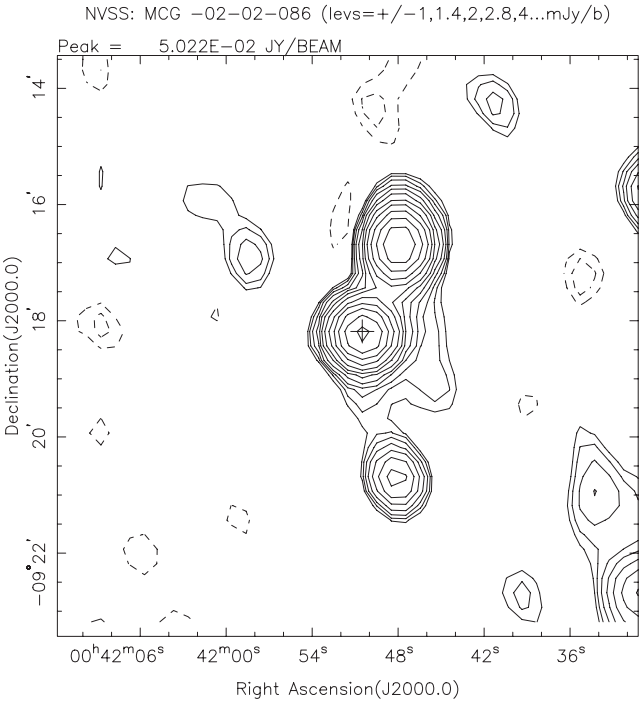

Figure A2. MCG-02-02-086 NVSS 10 × 10 arcmin^2 image.

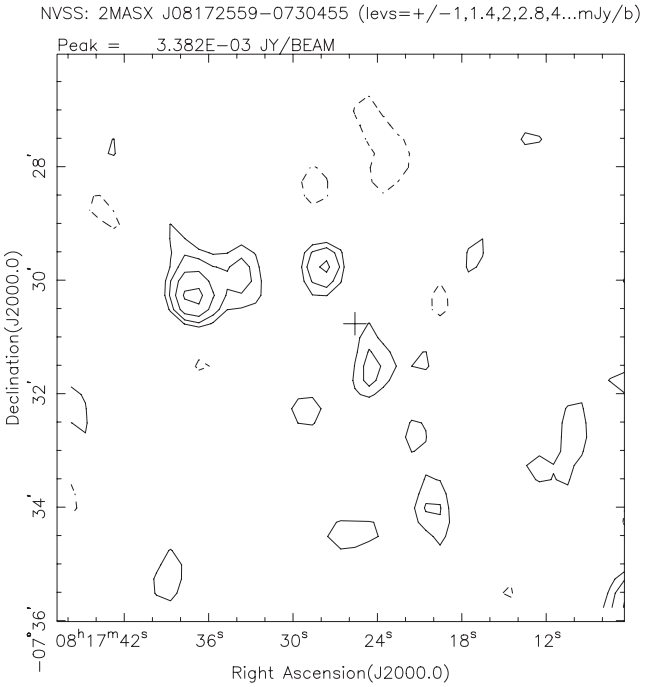

Figure A3. PGC 023233 NVSS 10 × 10 arcmin^2 image.

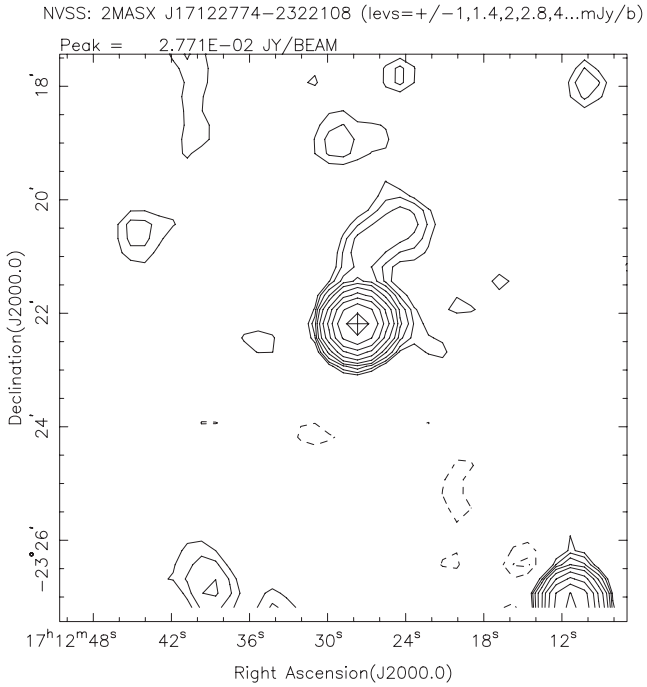

Figure A4. 2MASX J17122774−2322108 NVSS 10 × 10 arcmin^2 image.

SUPPORTING INFORMATION

Additional Supporting Information may be found in the online version of this article:

Table S1. Radial kinematics for ESO541-013.
Table S2. Radial kinematics for MCG-02-02-086.
Table S3. Radial kinematics for PGC023233.
Table S4. Radial kinematics for 2MASXJ17122774-2322108.
(http://mnras.oxfordjournals.org/lookup/suppl/doi:10.1093/mnras/stu020/-/DC1).

Please note: Oxford University Press are not responsible for the content or functionality of any supporting materials supplied by the authors. Any queries (other than missing material) should be directed to the corresponding author for the article.

This paper has been typeset from a TEX/LATEX file prepared by the author.